Acta Materialia 225 (2022) 117549

Contents lists available at ScienceDirect

Acta Materialia

journal homepage: www.elsevier.com/locate/actamat

Effect of hydrogen on evolution of deformation microstructure in low-carbon steel with ferrite microstructure

Kazuho Okada[a,*], Akinobu Shibata[a,b,c], Wu Gong[b,d], Nobuhiro Tsuji[a,b]

[a] Department of Materials Science and Engineering, Kyoto University, Yoshida-honmachi, Sakyo-ku, Kyoto 606-8501, Japan
[b] Elements Strategy Initiative for Structural Materials (ESISM), Kyoto University, Yoshida-honmachi, Sakyo-ku, Kyoto 606-8501, Japan
[c] Research Center for Structural Materials, National Institute for Materials Science (NIMS), 1-2-1 Sengen, Tsukuba 305-0047, Japan
[d] J-PARC Center, Japan Atomic Energy Agency, 2-4 Shirane Shirakata, Tokai-mura, Naka-gun, Ibaraki 319-1195, Japan

ARTICLE INFO

Article history:
Received 29 April 2021
Revised 6 December 2021
Accepted 6 December 2021
Available online 12 December 2021

Keywords:
Hydrogen embrittlement
Ferritic steel
Electron backscattered diffraction (EBSD)
Transmission electron microscopy (TEM)
Neutron diffraction

ABSTRACT

In this study, the deformation microstructure of hydrogen-charged ferritic-pearlitic 2Mn-0.1C steel was characterized using SEM-BSE, SEM-EBSD, TEM, and neutron diffraction. The microscopic mechanism of hydrogen-related quasi-cleavage fracture along the {011} planes was also discussed. It was found that hydrogen increased the relative velocity of screw dislocations to edge dislocations, leading to a tangled dislocation morphology, even at the initial stage of deformation ($e = 3\%$). In addition, the density of screw dislocations at the later stage of deformation ($e = 20\%$) increased in the presence of hydrogen. Based on the experimental results, it is proposed that a high density of vacancies accumulated along {011} slip planes by jog-dragging of screw dislocations, and coalescence of the accumulated vacancies led to the hydrogen-related quasi-cleavage fracture along the {011} slip planes.

1. Introduction

The premature fracture of metals and alloys induced by hydrogen is called 'hydrogen embrittlement,' 'hydrogen-related fracture,' or 'delayed fracture.' Several models have been proposed to account for hydrogen-related fractures. The proposed models are classified into two types depending on the mode of fracture, either brittle or ductile. High hydrogen pressure bubble or void [1,2] and hydrogen-enhanced decohesion (HEDE) [3–5] models consider hydrogen-induced brittle fracture, whereas hydrogen-enhanced localized plasticity (HELP) [6–8] and hydrogen-enhanced strain-induced vacancies (HESIV) [9,10] models are based on the idea that hydrogen promotes ductile fracture.

High-strength materials like martensitic steel are more susceptible to hydrogen embrittlement due to their increased strength. The introduction of a certain amount of hydrogen into steel during fabrication and application is inevitable, thus, hydrogen embrittlement has become a major issue in steel research.

Hydrogen-related quasi-cleavage fracture, which is a typical hydrogen-related fracture mode in martensitic steels, is a trans-granular fracture on a non-typical cleavage plane. The resultant fracture surface usually consists of serrated markings, which differ from typical river patterns on cleavage surfaces [11–15]. Kim et al. [16,17] and Nagao et al. [18] reported that hydrogen-related quasi-cleavage fracture occurred on the lath boundaries. On the other hand, Shibata et al. [19–21] performed precise crystallographic orientation analysis and revealed that the hydrogen-related quasi-cleavage fracture propagated parallel to the {011} planes within the lath. To understand the intrinsic characteristics of hydrogen-related quasi-cleavage fractures, we investigated the crystallographic features of hydrogen-related quasi-cleavage fracture surfaces in steel mainly composed of ferrite microstructures [22]. The results clearly demonstrated that the hydrogen-related quasi-cleavage fracture along the {011} planes was not due to the martensitic structure. Rather it was the intrinsic nature of the hydrogen-related quasi-cleavage fracture in steels with body-centered cubic (BCC) phases. Because the {011} plane corresponds to the slip plane in BCC crystals, further study on the effect of hydrogen on plastic deformation is needed to understand the mechanism of hydrogen-related quasi-cleavage fracture.

Tabata et al. [8] performed in situ TEM observations during tensile testing of pure iron under a hydrogen atmosphere and clarified that the dislocation motion around the crack tip was enhanced by the presence of hydrogen. Martin et al. [15] observed a deformed microstructure just beneath the hydrogen-related quasi-cleavage

* Corresponding author.
E-mail addresses: okada.kazuho.56z@st.kyoto-u.ac.jp (K. Okada), shibata.akinobu@nims.go.jp (A. Shibata), gong.wu@jaea.go.jp (W. Gong), nobuhiro-tsuji@mtl.kyoto-u.ac.jp (N. Tsuji).

https://doi.org/10.1016/j.actamat.2021.117549

fracture surface in pipeline steel and reported that voids initiated at and extended along the intersections between slip bands. Takai et al. [23] studied the effects of hydrogen and pre-strain on the hydrogen-related fractures of pure iron. The tensile-tested and unloaded hydrogen-charged specimens were aged at 30 °C to allow the hydrogen to diffuse out or annealed at 200 °C to eliminate strain-induced defects. The fracture strain of the hydrogen-diffused-out specimen was significantly smaller than that of the uncharged specimen in the reloading stage, while the stress–strain behavior of the specimen in which the defects were eliminated was similar to that of the uncharged specimen. Based on the results, it was proposed that the introduction of vacancies during hydrogen-related deformation was a key factor in hydrogen embrittlement rather than hydrogen itself. Although several studies, such as those described above, have reported the effect of hydrogen on plastic deformation, it is still unclear how the accelerated plastic deformation due to hydrogen leads to quasi-cleavage fracture.

In this study, we characterized the evolution of the deformation microstructure in a hydrogen-charged steel with ferrite (and a small amount of pearlite) microstructure. The microscopic mechanism of hydrogen-related quasi-cleavage fracture along {011} slip planes is also discussed in terms of the acceleration of plastic deformation by hydrogen.

2. Experimental

A 2Mn-0.1C (mass%) steel with ferrite and pearlite phases was used in the present study. The detailed chemical composition (wt.%) is C: 0.103, Mn: 2.03, Si: 0.01, P: <0.002, S: 0.0010, and Fe: bal. The as-cast ingot of the 2Mn-0.1C steel was cold-rolled from 15 mm to 1.5 mm in thickness and austenitized at 1173 K for 1.8 ks under vacuum, followed by furnace cooling. Then, the specimens were mechanically ground to a thickness of 1 mm to remove the decarburized layers formed during the heat treatment. Sheet-type tensile test specimens with a gage length of 10 mm, a width of 5 mm, and a thickness of 1 mm were cathodically pre-charged with hydrogen in an aqueous solution of 3% NaCl + 3 g L^{-1} NH_4SCN at a current density of 5 A m^{-2}. The diffusible hydrogen content measured by thermal desorption analysis was 0.16 wt. ppm. Uniaxial tensile tests were then performed at a strain rate of 8.3×10^{-6} s^{-1}, at ambient temperature under hydrogen concurrent-charging conditions (same as the pre-charging condition). The microstructure and thermal desorption analysis results are presented in our previous paper [22]. Some of the tensile tests were stopped and the specimens were unloaded at strain amounts of 3%, 11.5%, 20%, and 24%, corresponding to the end of the Lüders deformation, the middle point of work hardening, the ultimate tensile strength, and prior to final rupture, respectively.

The microstructure of the tensile-tested specimens was characterized by analyzing data from neutron diffraction, scanning transmission electron microscopy (STEM, JEOL: JEM-2100F), backscattering electron (BSE) images using scanning electron microscopy (SEM, JEOL: JSM-7800F), and electron backscattering diffraction (EBSD, JEOL: JSM-7100F). To obtain the average macroscopic information of the deformation microstructure, the tensile-tested and unloaded specimens at strain amounts of 3%–20% were analyzed by neutron diffraction using BL19 “TAKUMI” in the Materials and Life Science Experimental Facility (MLF) of the Japan Proton Accelerator Research Complex (J-PARC). The irradiated area of the neutron beam was 5 mm square. From the obtained neutron diffraction profiles, the dislocation densities and the fractions of screw/edge dislocations were evaluated by a convolutional multiple whole profile (CMWP) fitting proposed by Ungar [24–26]. The fractions of screw and edge dislocations were determined from parameter q obtained from CMWP fitting. Parameter q has to be in between 1.29 (for 100% edge) and 2.64 (for 100% screw) in BCC steels [27]. The microscopic dislocation morphologies were characterized using STEM at an acceleration voltage of 200 kV. Disks having a diameter of 1.5 mm were cut from the specimens used for the neutron diffraction experiments and mechanically ground to 30–40 μm in thickness, followed by electropolishing in a solution of 10% $HClO_4$ + 90% CH_3COOH at ambient temperature. For the BSE and EBSD analyses, a Ni layer was electrodeposited onto the tensile-tested specimens at a strain amount of 24% to preserve the hydrogen-related crack surfaces. Electrodeposition was conducted in an aqueous solution of 150 g L^{-1} Ni_2SO_4 + 15 g L^{-1} H_3BO_4 at ambient temperature with a current density of 30 Am^{-2} for 265.6 ks. Then, the mid-thickness sections of the electrodeposited specimens were analyzed using BSE and EBSD. The surfaces of the specimens for BSE observations and EBSD measurements were prepared by vibration polishing with a 0.02 μm colloidal silica suspension. EBSD measurements and analyses were performed using the TSL OIM Data Collection and the TSL OIM Analysis programs, respectively.

3. Results

3.1. Neutron diffraction results

Fig. 1 shows the neutron diffraction profiles (black) and the CMWP fitting results (red) of (a, c and e) uncharged specimens and (b, d and f) hydrogen-charged specimens ((a and b) e = 3%, (c and d) e = 11.5%, and (e and f) e = 20%). The difference between the measured data and the fitted pattern is shown in blue lines. The R_{wp} of every fitting result were below 2%, though the 110 peak tails of the fitted patterns were slightly deviated from the experimentally measured profiles. The R_{wp} is the most significant agreement factor of CMWP fitting and it has value below 12% for typical adequate refinement [28]. Therefore, we can say that all the fitting results are plausible. Fig. 2 shows the nominal stress–nominal strain curves (adapted from [22]) and dislocation densities of the uncharged specimens (black, circle marks) and the hydrogen-charged specimens (red, triangle marks). Although the total elongation of the hydrogen-charged specimen (27%) is much smaller than that of the uncharged specimen (48%), the dislocation densities are hardly affected by the presence of hydrogen at the corresponding strain amounts. Fig. 3(a) shows the fractions of screw and edge dislocations estimated from the neutron diffraction analysis, where the triangle marks and the circle marks correspond the hydrogen-charged and uncharged specimens, respectively. The left and right axes indicate the fractions of the edge and screw components, respectively. In the uncharged specimens, almost all of the dislocations were screw-type at the initial stage of deformation (e = 3%), and the fraction of the edge component increased monotonically with increasing strain. In contrast, almost equal fractions of screw and edge components were present that did not vary greatly with the strain amount in the hydrogen-charged specimens. From the dislocation density data (Fig. 2) and the fractions of the dislocations (Fig. 3(a)), we calculated the individual densities of each type of dislocations. Fig. 3(b) and (c) show the changes in the screw and edge dislocation densities with strain amount. We found that the screw dislocation density in the hydrogen-charged specimen was much higher than that of the uncharged specimen at the later stage of deformation (e = 20%).

A certain amount of dislocations that form cell boundaries are excluded in the neutron diffraction results shown in Figs. 2 and 3, because their elastic strain fields mutually cancel each other. Ungar and Mughrabi et al. [29] demonstrated that the densities of total dislocations (existing outside the cell boundaries and constituting cell boundaries) measured by X-ray diffrac-

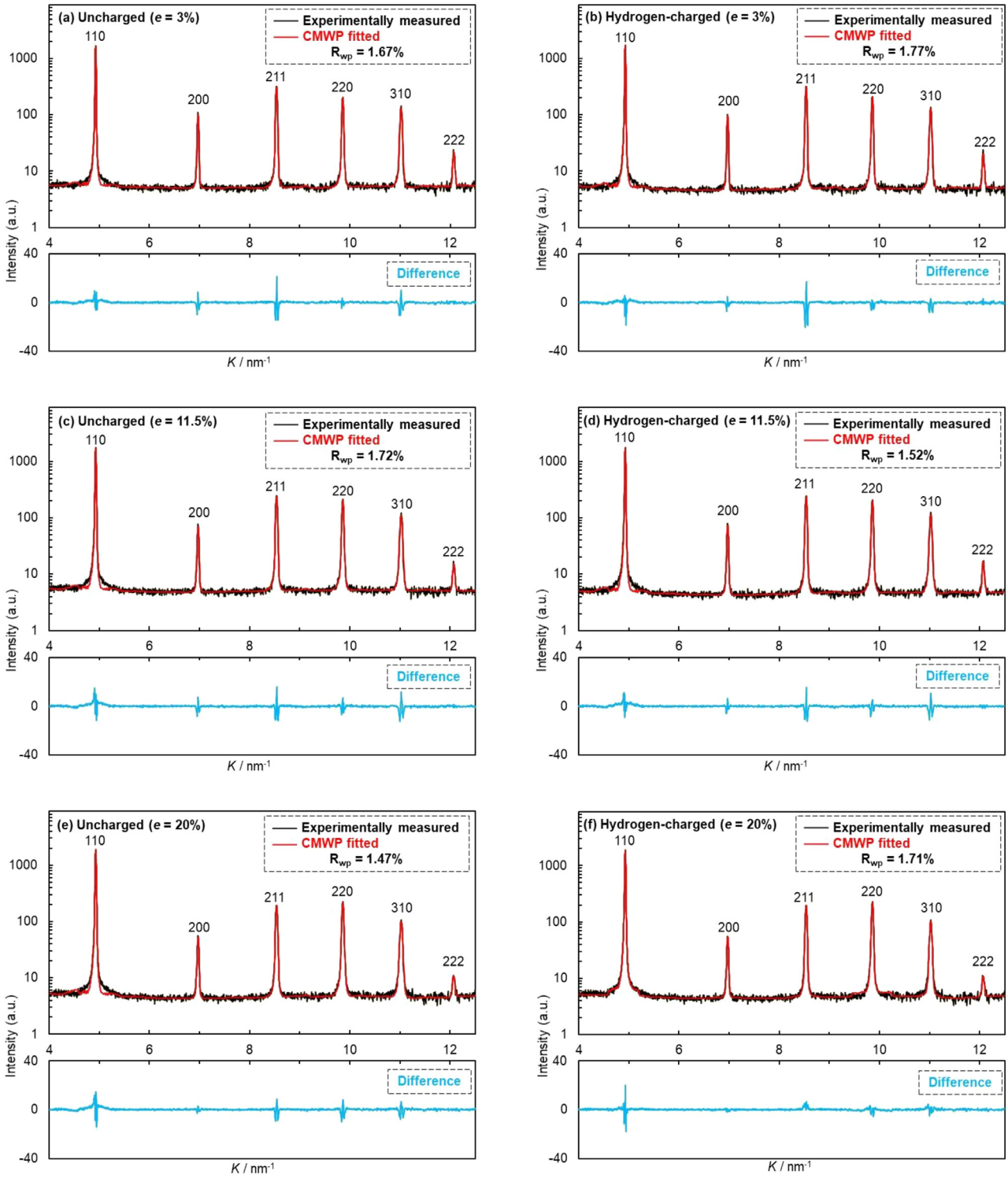

Fig. 1. The neutron diffraction profiles (black) and the CMWP fitting results (red) of (a, c and e) uncharged specimens and (b, d and f) hydrogen-charged specimens ((a and b) $e = 3\%$, (c and d) $e = 11.5\%$, and (e and f) $e = 20\%$). The difference between the measured data and the fitted pattern is shown in blue lines.

tion experiment and TEM observation were well consistent. In contrast, underestimated dislocation densities due to the difficulty of counting all the dislocations constituting cell boundaries in TEM observation [30] and the cancelation of elastic fields of dislocation dipole and multi-pole in diffraction method [31] were reported. Dislocations that form cell boundaries are also closely related with crystallite size which is estimated in the CMWP.

3.2. STEM observation results

Fig. 4 shows low magnification STEM images of the dislocation morphologies in (a and b) the uncharged specimens and (c and d) the hydrogen-charged specimens. The incident electron beam directions for all of the images are ~<111> and the two-beam conditions are satisfied ($\mathbf{g} = 011$). The dislocation morphology of the uncharged and hydrogen-charged specimens are significantly dif-

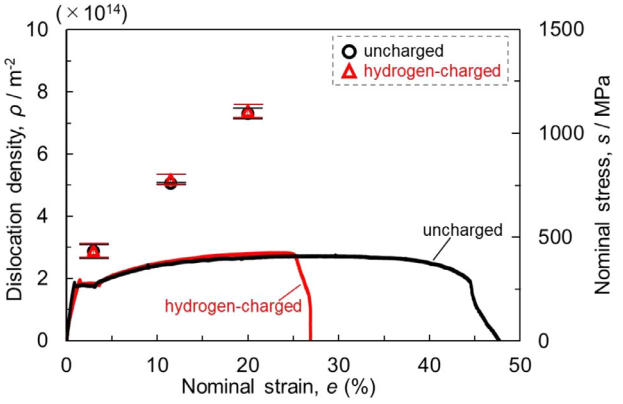

Fig. 2. Nominal stress–nominal strain curves and dislocation densities of the uncharged specimens (black, circle marks) and the hydrogen-charged specimens (red, triangle marks). Nominal stress–nominal strain curves are adapted from [22].

ferent even at the initial stage of deformation (e = 3%). The dislocations are linear in the uncharged specimen (Fig. 4(a)), while they are curved and tangled in the hydrogen-charged specimen (Fig. 4(c)). The tangled dislocation morphology in the hydrogen-charged specimen was also observed previously [32]. At the later stage of deformation (e = 20%), we can recognize the well developed dislocation cell structures in both the uncharged (Fig. 4(b)) and hydrogen-charged specimens (Fig. 4(d)). In this study, the cell structures will be reffered to as low energy dislocation structures (LEDS). The size of the LEDS in the hydrogen-charged specimen tends to be smaller than that in the uncharged specimen.

To further investigate the deformation microstructure, the nature of the dislocations was characterized. Fig. 5(a)–(c) show STEM images from the same area with different diffraction vectors in the uncharged specimen at a strain amount of 3%. The Kikuchi diffraction patterns presented on the right side of the images demonstrate that the two-beam condition is satisfied when the diffraction vectors are (a) $\boldsymbol{g}$ = 011, (b) $\boldsymbol{g}$ = −110, and (c) $\boldsymbol{g}$ = 101. Considering the {011} <111> slip system in the BCC crystal, dislocations with four types of Burgers vectors can exist: $\boldsymbol{b}$ = a/2[11–1], a/2[1–1–1], a/2[111], and a/2[−11–1]. According to the $\boldsymbol{g}\cdot\boldsymbol{b}$ = 0 invisibility criterion, the dislocations having two out of four types of Burgers vectors are visible in each STEM image, which are listed at the top of each image. The orientations of the Burgers vectors are indicated by black arrows in the stereographic projections. Fig. 5(d) shows a schematic illustration of the dislocation configurations where the Burgers vectors of the dislocations determined by contrast analysis using (a)–(c) are represented by different colors (red: a/2[111], blue: a/2[1–1–1], green: a/2[−11–1], and gray: a/2[11–1]). The dislocations with $\boldsymbol{b}$ = a/2[11–1] are invisible in all the STEM images of (a)–(c) because the incident electron beam direction is nearly parallel to [11–1]. Although we can simply assume that the straight dislocations have a large screw component, the inclination of the dislocation lines with respect to the paper depth direction is difficult to identify from the two-dimensional image. Fig. 6(a) shows a STEM image after tilting the specimen by 23.5° from the condition of Fig. 5(a), maintaining the same two-beam condition ($\boldsymbol{g}$ = 011). The result of the two-surface trace analysis for the straight dislocation indicated by the white arrow is shown in Fig. 6(b). The plane traces, which include projected dislocation line vectors (square marks) and incident electron beam directions (circle marks) in Figs. 5(a) and 6(a), are drawn in the solid and broken lines, respectively. Because the true line vector of the dislocation should lie on both planes (the solid and broken lines), the true line vector of the dislocation is determined to be [0.489 0.617 0.617]. The angle between the line vector (the red cross mark) and the Burgers vector (the red triangle mark) of the dislocation is 5.96° Thus, we can consider that the observed straight dislocation has a large screw component. Through two-surface trace analyses for several dislocations, we confirmed that almost all of the straight dislocations in the uncharged specimen (e = 3%) had a large screw component.

Fig. 7 shows that the dislocations at the later stage of deformation (e = 20%) were curved and tangled in comparison to those at the initial stage (Fig. 5). The curved and tangled dislocation morphology resulted in an increase in the edge component. The STEM analyses of the uncharged specimens shown above are consistent with the results of neutron diffraction analysis (Fig. 3), where the fraction of the screw component was very large (∼97%) at the initial stage of deformation, and the edge component increased with increasing strain.

The dislocation configuration in the hydrogen-charged specimen at the initial stage of deformation (e = 3%) is presented in Fig. 8. The dislocations appeared to be more tangled compared to that of the uncharged specimen (Fig. 5). In addition, many dislocation components lie nearly perpendicular to their Burgers vectors, as indicated by the arrows in Fig. 8(d). This implies that these dislocation components comprise almost purely of edge dislocations. These features are consistent with the neutron diffraction results shown in Fig. 3(a). For dislocations with a large edge component, the crystallographic orientation of the slip plane can be determined by the cross product of the Burgers vector and the dislocation line vector. The Burgers vectors and line vectors of dislocation segments indicated by arrows (A–L) in Fig. 8(d) were determined by contrast analysis and two-surface trace analysis, respectively. The derived slip plane normal orientations of the disloca-

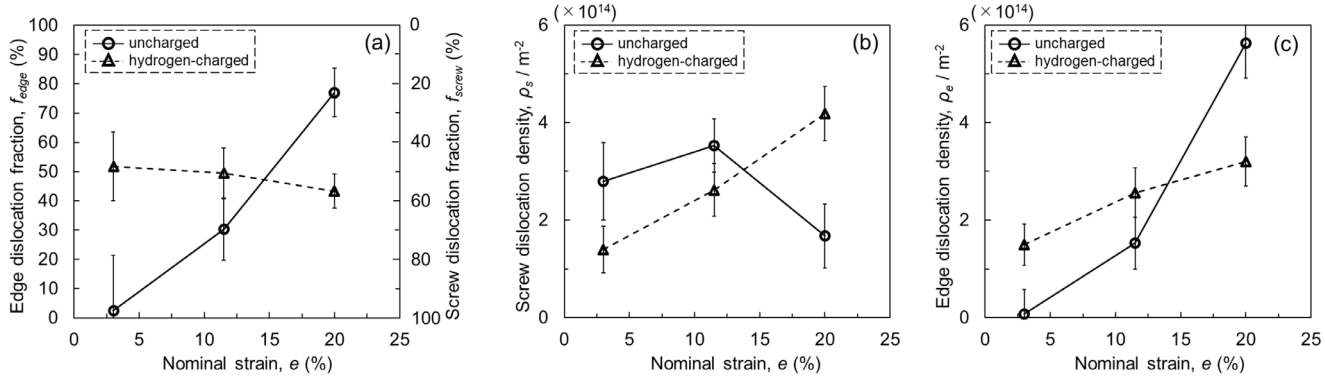

Fig. 3. (a) Fractions of screw and edge dislocations, (b) screw dislocation densities, and (c) edge dislocation densities of the uncharged specimens (solid lines, circle marks) and the hydrogen-charged specimens (broken lines, triangle marks) plotted as a function of nominal strain.

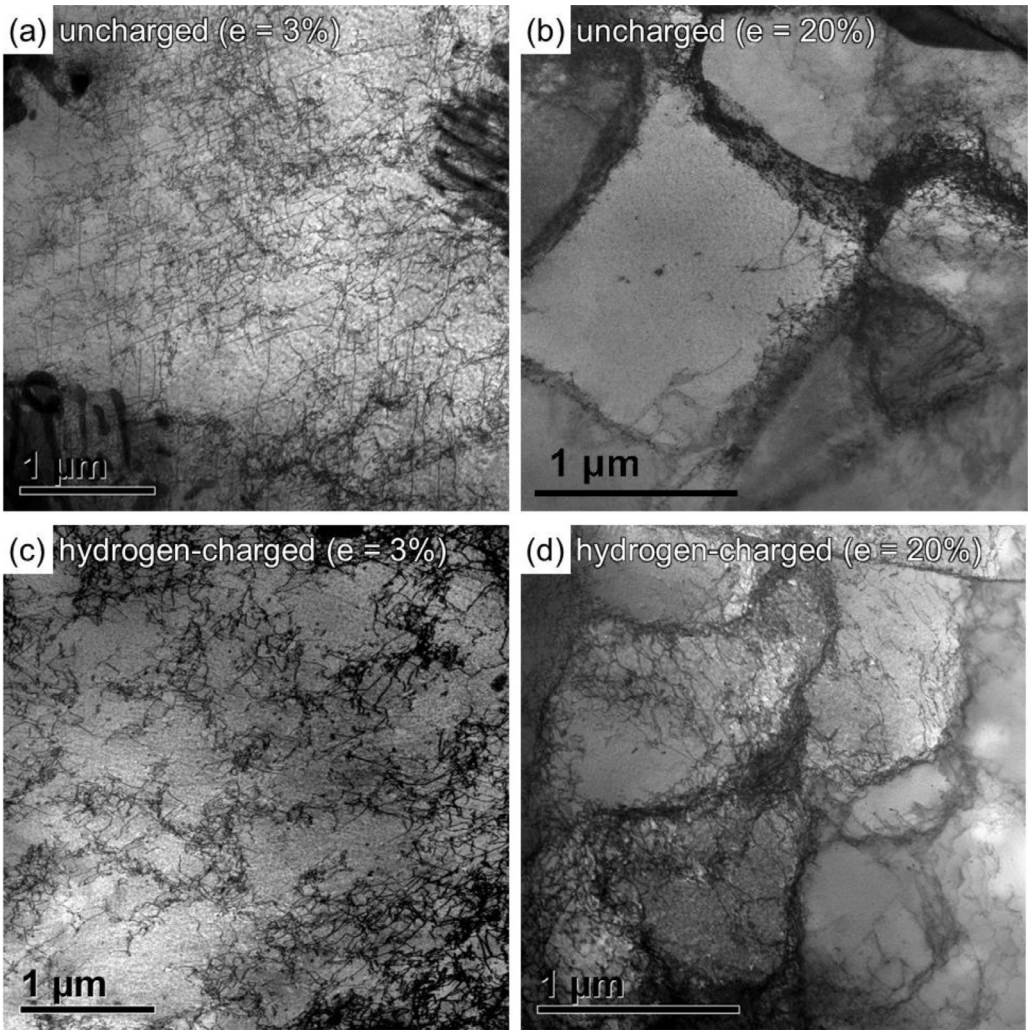

Fig. 4. Low magnification STEM images of the dislocation morphologies in (a and b) the uncharged specimens and (c and d) the hydrogen-charged specimens. The strain amounts of (a and c) and (b and d) are 3% and 20%, respectively. The incident electron beam directions for all of the images are ~<111> and two beam conditions are satisfied ($\boldsymbol{g} = 011$).

tion segments are plotted on a stereographic triangle, as shown in Fig. 9. Because the slip plane orientations of 9 out of 12 dislocation segments are almost parallel to the {011} plane, we can conclude that the dominant slip system of the hydrogen-charged specimen is {011} <111>. STEM images with different diffraction vectors and a corresponding dislocation configuration in the hydrogen-charged specimen at the later stage of deformation ($e = 20\%$) are presented in Fig. 10. In contrast to the uncharged specimen (Fig. 7), many straight dislocations whose line vectors are nearly parallel to their Burgers vectors can be observed, as indicated by the white arrows in Fig. 10(d). These straight dislocations would be the origin of the higher screw dislocation density in the hydrogen-charged specimen at the later stage of deformation (Fig. 3(b)). As described above, the results of the STEM observations are consistent with the neutron diffraction analysis results.

3.3. SEM observation results

Fig. 11 shows (a, c and e) SEM-BSE images and (b, d and f) corresponding boundary maps obtained by EBSD orientation analysis in the specimens that were tensile-deformed to 24%; (a and b) the uncharged specimen, (c–f) the hydrogen-charged specimen. In the boundary maps, the LEDS boundaries are drawn by different colors depending on the misorientation angle. A large crack propagated at the strain amount in the hydrogen-charged specimen (Fig. 13, the details are explained later), while no crack was observed in the uncharged specimen. Fig. 11(c) and (d) show the microstructure of the region 1 mm from the crack tip in the direction parallel to the tensile axis, and the observed region of Fig. 11(e) and (f) is just beneath the crack surface. We can regard the region beneath the crack surface as that beneath the quasi-cleavage surface because over 90% area of the fracture surface was covered by quasi-cleavage surface in the hydrogen-charged specimen [22]. Previous studies reported that the evolution of deformation microstructure strongly depends on the crystallographic orientation with respect to the tensile direction [33–36]. In order to consider only the effect of hydrogen, we observed the grains having nearly the same orientations; the crystallographic orientations of the tensile direction and the observed direction are almost the same in all the three observed grains as presented in Fig. 11(g). It was observed that the size of LEDS tends to be smaller and the misorientation of LEDS is larger in the hydrogen-charged specimen than those in the uncharged specimen. The statistical size distributions of LEDS and misorientation distributions of LEDS boundaries are summarized in Fig. 12(a) and (b), respectively. We analyzed more than 600 LEDSs in each area. The $d_{LEDS\text{-}ave}$ and the $\theta_{LEDS\text{-}ave}$ represent the average size of LEDS and the average misorientation of LEDS boundaries in each observed area. As shown in Fig. 12(a), the $d_{LEDS\text{-}ave}$ in

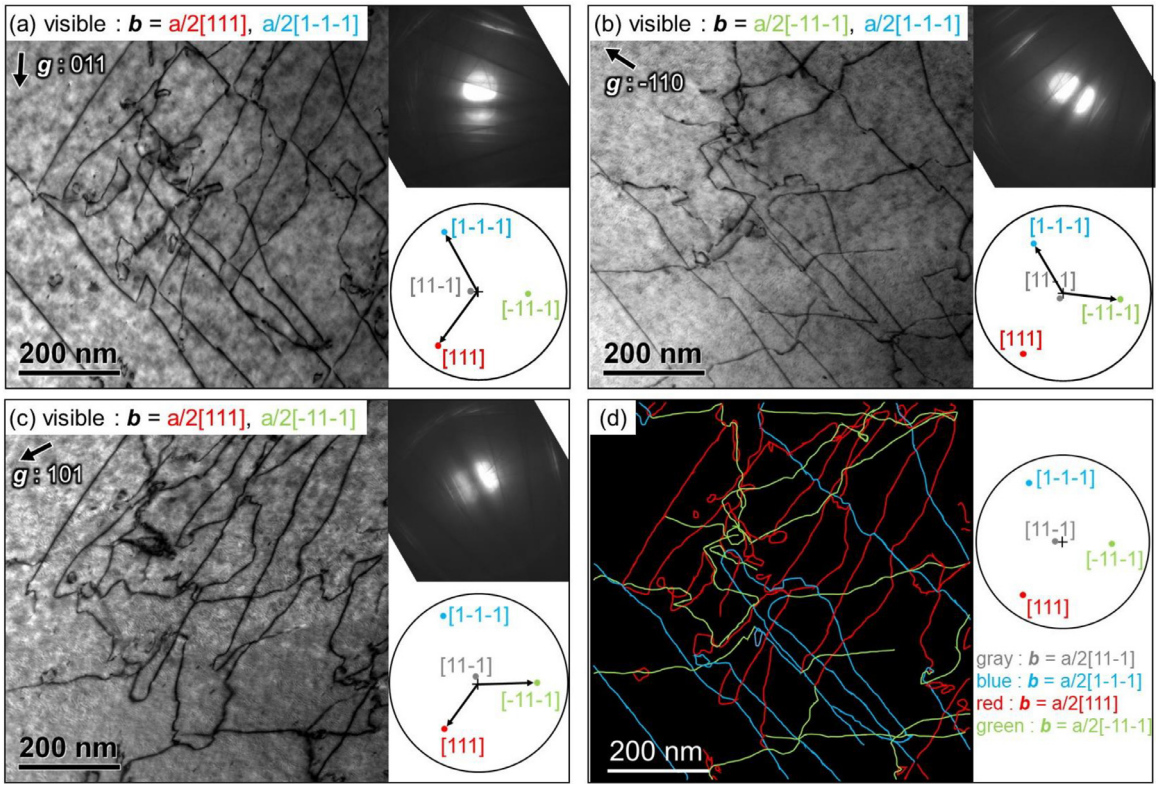

Fig. 5. (a–c) High magnification STEM images with different diffraction vectors under two-beam conditions in the uncharged specimen at a strain amount of 3%. The Kikuchi diffraction patterns are presented at the right side of the images; (a) $\boldsymbol{g} = 011$, (b) $\boldsymbol{g} = -110$, and (c) $\boldsymbol{g} = 101$. (d) Schematic illustration of the dislocation configurations where the Burgers vectors of the dislocations determined by contrast analysis using (a)–(c) are represented by different colors (red: a/2[111], blue: a/2[1–1–1], green: a/2[−11–1], and gray: a/2[11–1]).

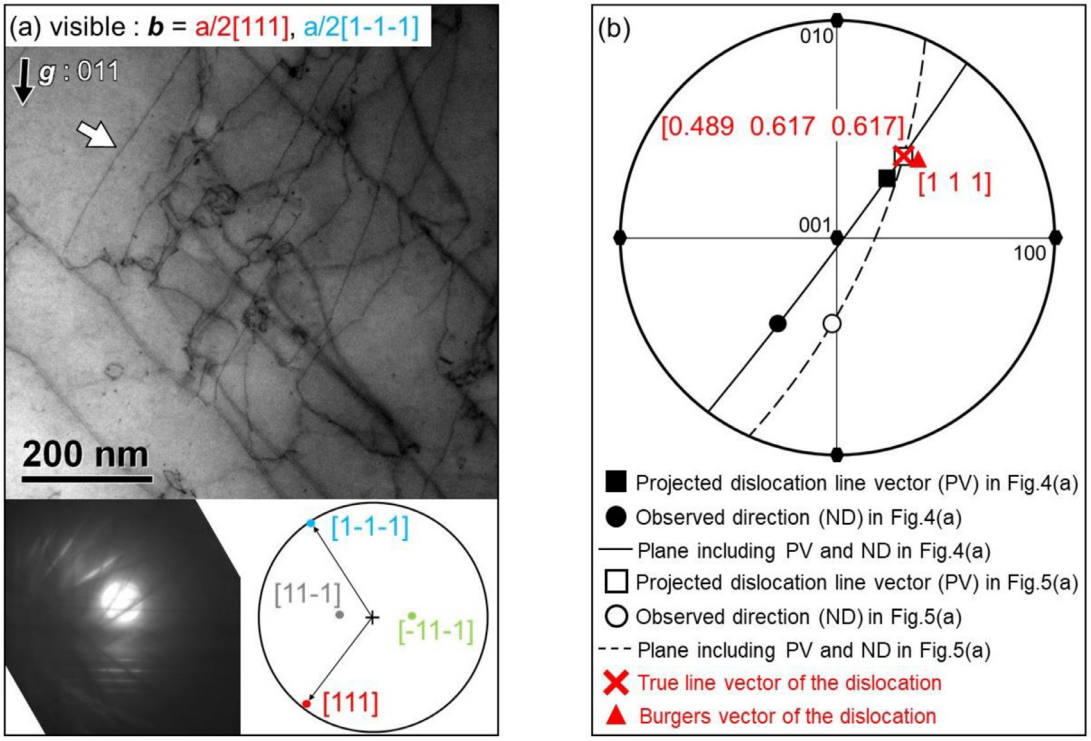

Fig. 6. (a) STEM image after tilting the specimen by 23.5° from the condition shown in Fig. 5(a) while maintaining the same two-beam condition ($\boldsymbol{g} = 011$). (b) Stereographic projection showing the result of two-surface trace analysis for the straight dislocation indicated by the white arrow in (a).

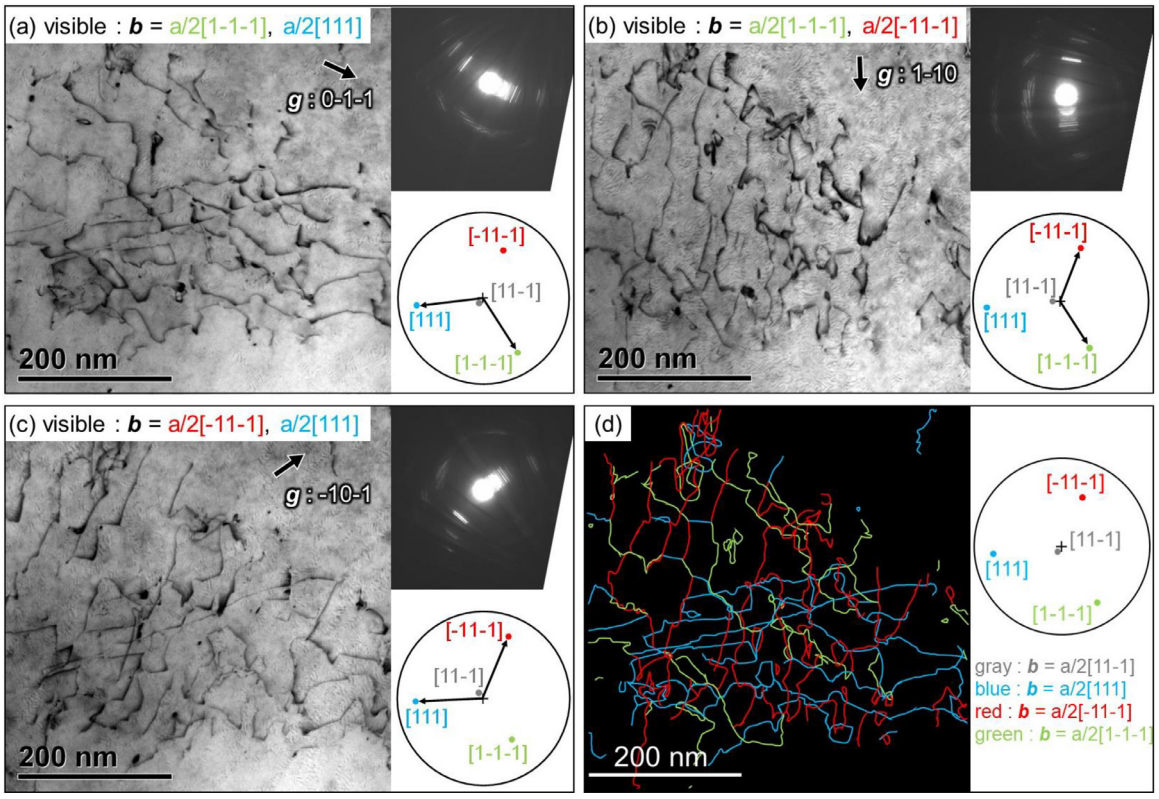

Fig. 7. (a–c) STEM images with different diffraction vectors under two-beam conditions ((a) $\boldsymbol{g} = 0\text{–}1\text{–}1$, (b) $\boldsymbol{g} = 1\text{–}10$, and (c) $\boldsymbol{g} = -10\text{–}1$) in the uncharged specimen at the later stage of deformation ($e = 20\%$), and (d) corresponding schematic illustration of the dislocation configurations where Burgers vectors of the dislocations were determined by contrast analysis using STEM images of (a)–(c).

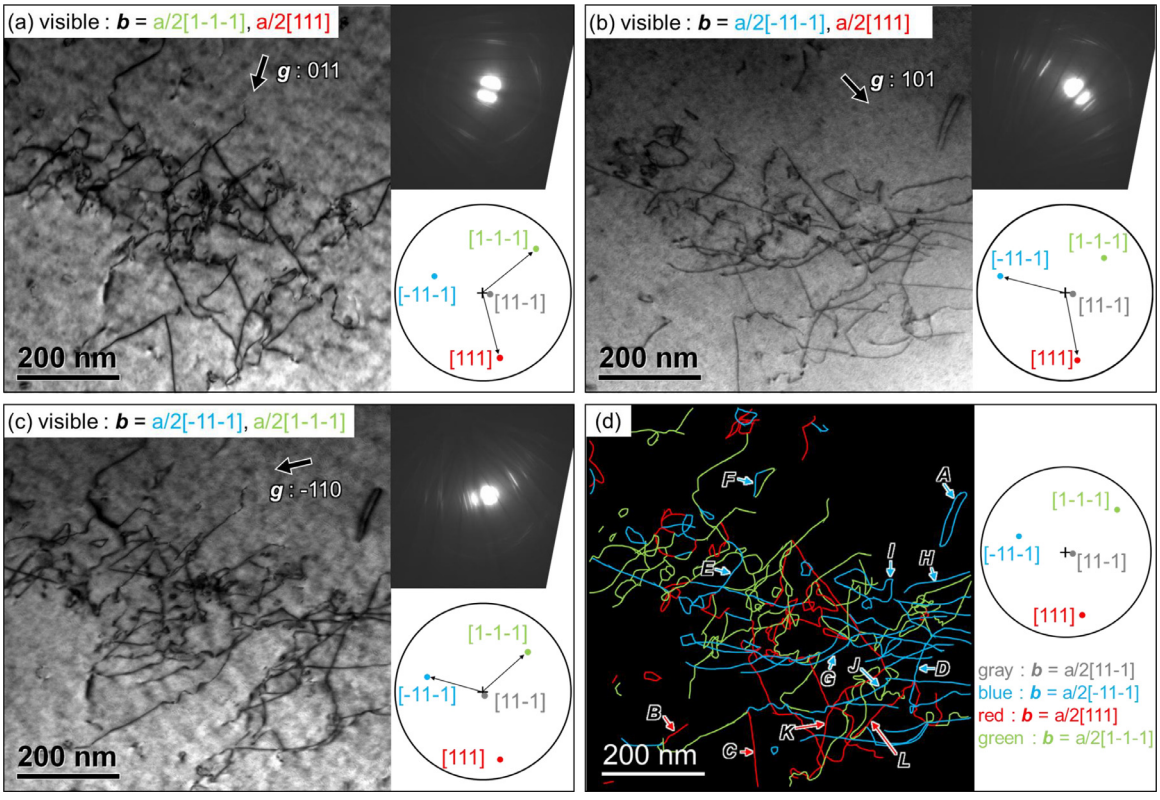

Fig. 8. (a–c) STEM images with different diffraction vectors under two-beam conditions ((a) $\boldsymbol{g} = 011$, (b) $\boldsymbol{g} = 101$, and (c) $\boldsymbol{g} = -110$) in the hydrogen-charged specimen at the initial stage of deformation ($e = 3\%$), and (d) corresponding schematic illustration of the dislocation configurations where Burgers vectors of the dislocations were determined by contrast analysis using STEM images of (a)–(c).

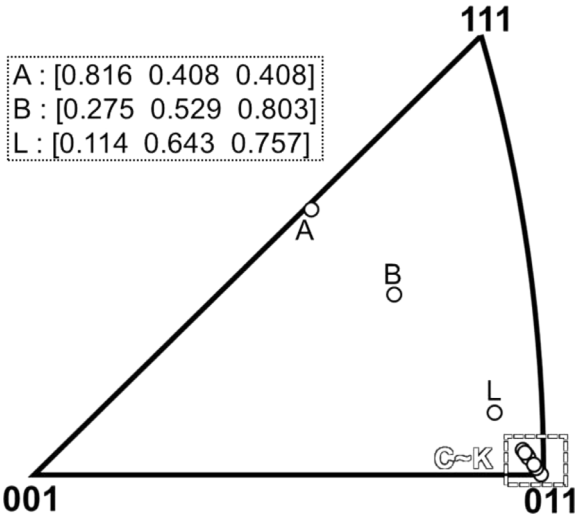

Fig. 9. Stereographic triangle showing the crystallographic orientation of slip plane normal of the dislocation segments with a large edge component which are indicated by arrows (A–L) in Fig. 8(d).

the regions 1 mm from the crack tip and just beneath the quasi-cleavage surface of the hydrogen-charged specimen are 0.510 μm and 0.359 μm, respectively, which are significantly smaller than that of the uncharged specimen ($d_{LEDS\text{-}ave}$ = 0.795 μm). The sizes of LEDSs observed using STEM (Fig. 4(b) and (d)) were well consistent with $d_{LEDS\text{-}ave}$ both in the uncharged and hydrogen-charged (1 mm from crack tip) specimens. In addition, the $\theta_{LEDS\text{-}ave}$ in the region 1 mm from the crack tip is 7.06°, much larger than that of the uncharged specimen (2.75°). However, the $\theta_{LEDS\text{-}ave}$ in the region just beneath the quasi-cleavage surface (2.84°) is similar to that of the uncharged specimen. A previous study [37] also reported the significantly small misorientation of LEDS boundaries just beneath the fracture surface for hydrogen-related fatigue fracture of ferritic-pearlitic steel. Generally, the size of LEDS decreases and misorientation of the LEDS boundaries increases with an increase in the strain [38–41]. Even though the local strain of the region close to the fracture surface is expected to be higher than the other areas, the misorientation of LEDS just beneath the quasi-cleavage surface is almost the same as that of the uncharged specimen. The effects of hydrogen on LEDS formation were extensibly studied in nickel-base metals and alloys [42–46]. Their results indicated that LEDS size was smaller under the presence of hydrogen in face-centered cubic (FCC) structures.

4. Discussion

As shown in Fig. 2, the dislocation densities of the hydrogen-charged and uncharged specimens obtained from diffraction experiments were similar at each strain amount. As explained previously, a certain amount of dislocation constituting the LEDS boundaries were not involved in the dislocation densities and characters derived from the neutron diffraction analysis, because their elastic strain fields mutually cancel each other. However, considering that the size of LEDS was smaller and the misorientation of LEDS boundaries was equal or larger in the hydrogen-charged specimen than those in the uncharged specimen (Fig. 12), we can safely assume that the amount of dislocation constituting LEDS boundaries was larger in the hydrogen-charged specimen. Therefore, the amount of excluded dislocation in the neutron diffraction analysis should be larger in the hydrogen-charged specimen and the density of total dislocations (existing outside the LEDS boundaries and constituting LEDS boundaries) was higher in the hydrogen-charged specimen.

It is widely accepted that in BCC steels [47–50], and more generally in BCC transition metals [51,52], edge dislocations have

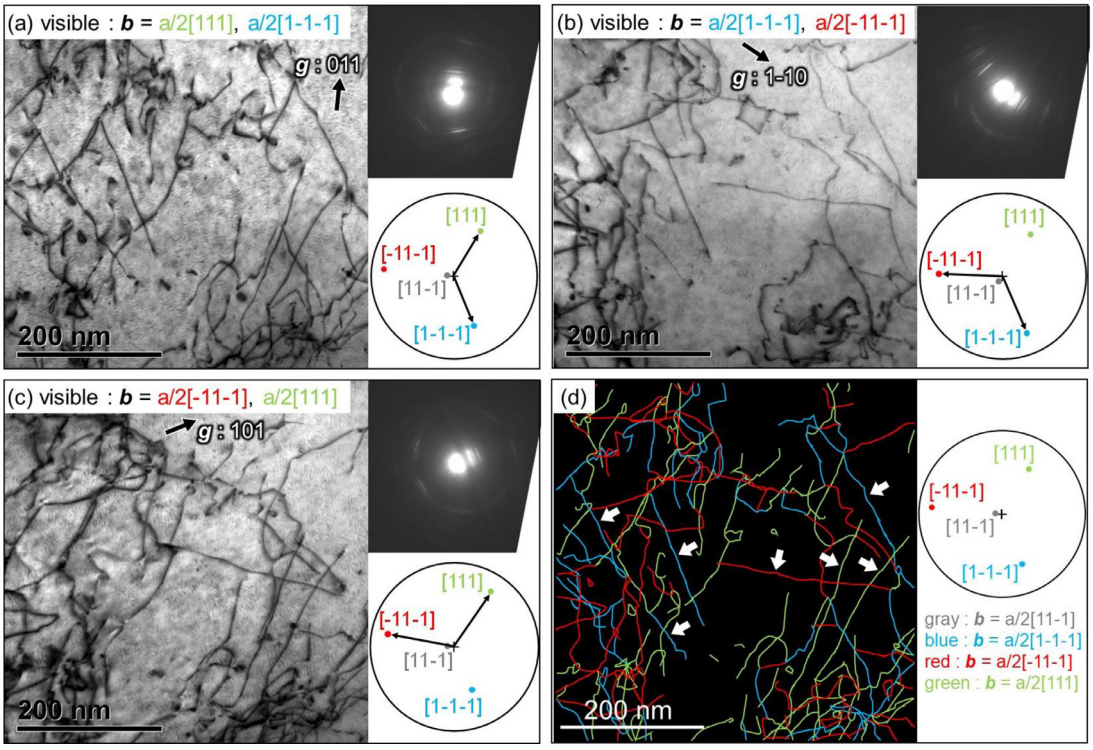

Fig. 10. (a–c) STEM images with different diffraction vectors under two-beam conditions ((a) $\boldsymbol{g}$ = 011, (b) $\boldsymbol{g}$ = 1–10, and (c) $\boldsymbol{g}$ = 101) in the hydrogen-charged specimen at the later stage of deformation (e = 20%), and (d) corresponding schematic illustration of the dislocation configurations where Burgers vectors of the dislocations were determined by contrast analysis using STEM images of (a)–(c).

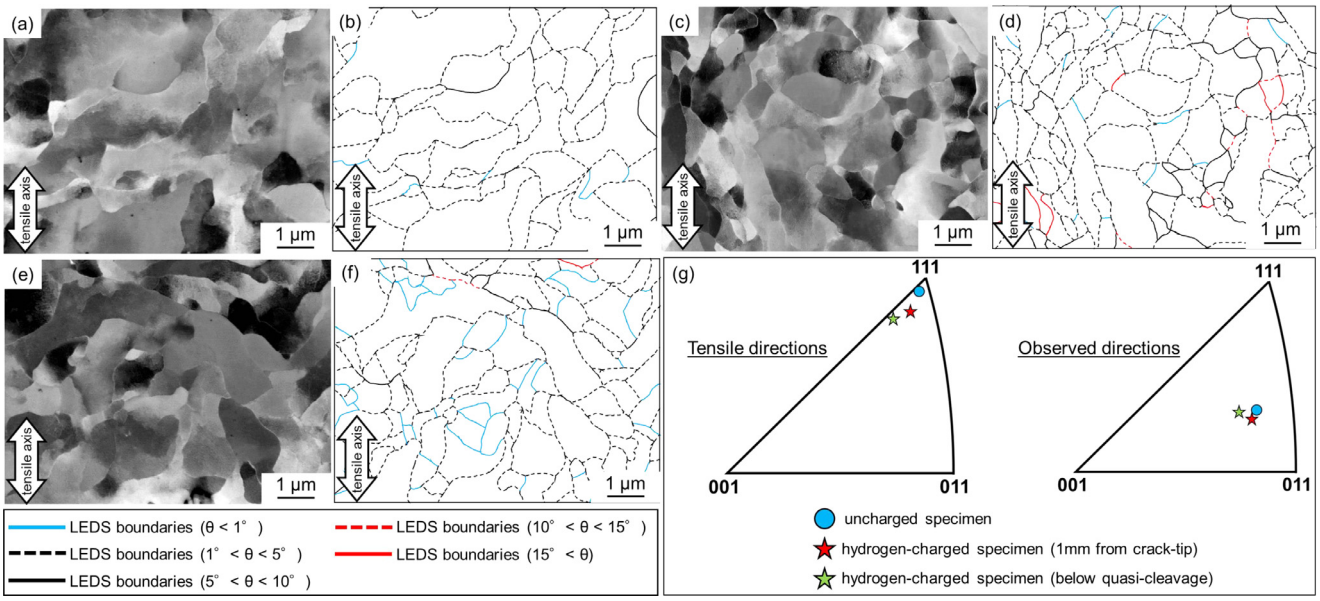

Fig. 11. (a, c and e) BSE images and (b, d and f) corresponding boundary maps obtained by EBSD orientation analysis in the specimens under tensile strain to 24%; (a and b) the uncharged specimen, (c and d) 1 mm from the crack tip in the hydrogen-charged specimen, and (e and f) just beneath the quasi-cleavage surface in the hydrogen-charged specimen. (g) Stereographic triangles showing the crystallographic orientation of the tensile directions and the observed directions in (a–f).

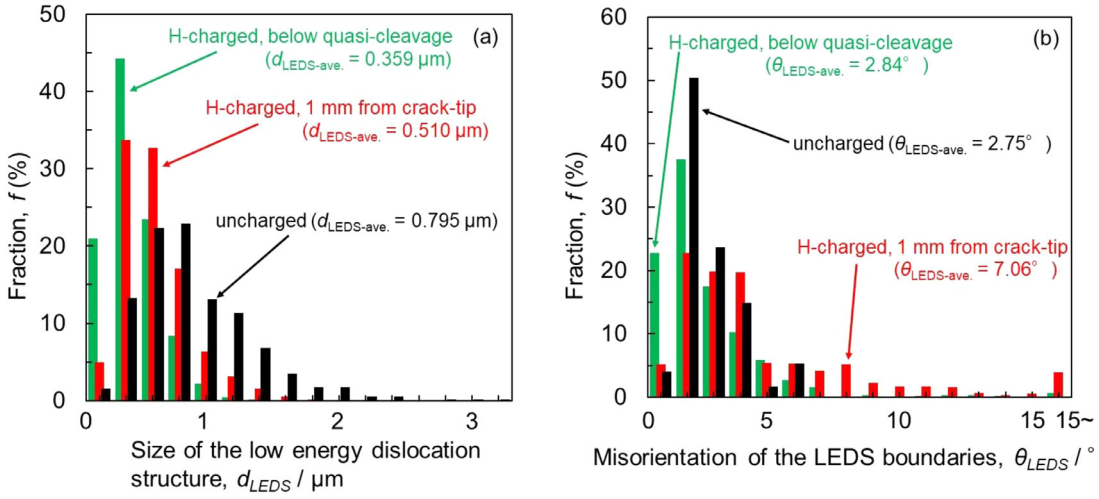

Fig. 12. (a) Statistical size distribution of LEDS and (b) statistical misorientation distribution of LEDS boundaries of the microstructures in Fig. 11. The red, green, and black bars indicate areas 1 mm from the crack tip in the hydrogen-charged specimen, just beneath the quasi-cleavage surface in the hydrogen-charged specimen, and the uncharged specimen, respectively. The $d_{LEDS-ave}$ and the $\theta_{LEDS-ave}$ represent the average size of LEDS and the average misorientation of LEDS boundaries in each observed area, respectively.

greater mobility than screw dislocations because of the higher Peierls potential of screw dislocations. Caillard [53] performed in situ TEM observation during tensile straining using uncharged pure Fe and confirmed that a dislocation loop evolved to a screw-segment-elongated morphology due to the relatively larger velocity of the non-screw segment. A similar screw-segment-elongated dislocation morphology was also observed in the analyzed uncharged ferritic steel (e = 3%) (Figs. 4(a), 5 and 6). On the other hand, the dislocation morphology became more curved and tangled during work hardening, leading to an increasing fraction of the edge component with an increase in the strain amount in the uncharged specimen (Figs. 3(a) and 7).

In the hydrogen-charged specimen, the fraction of the edge component was larger than that of the uncharged specimen at the initial stage of deformation (Fig. 3(a)). Through STEM observations, we demonstrated that the larger fraction of edge dislocations was due to the curved and tangled dislocation morphology (Fig. 8). The dislocation morphology with edge-segment-elongated dislocation loops like dislocation loop A shown in Fig. 8 is different from the screw-segment-elongated morphology in the uncharged specimen (Figs. 5 and 6). Thus, the observation results strongly suggest that relative velocity of screw dislocation to edge dislocation was increased by hydrogen. To understand the origin of the dislocation morphology in the hydrogen-charged specimen, it is necessary to consider the effect of hydrogen on screw and edge dislocations separately. Birnbaum and Sofronis [7] calculated the elastic interaction between hydrogen atoms and edge dislocations and proposed that hydrogen reduced the elastic interaction between edge dislocations and increased their mobility (hydrogen elastic shielding mechanism). However, some of the parameters used (diffusible hydrogen content: larger than 10^3 atm ppm, distance between two edge dislocations: smaller than 20***b***) are notably different from

the experimental condition in this study; the diffusible hydrogen content and the average dislocation distance were 8.9 atm ppm (0.16 wt ppm) and 237***b***, respectively (based on the hypothesis that hydrogen atoms and dislocations were distributed uniformly at the initial stage of deformation). Hydrogen elastic shielding mechanism was demonstrated by some three-dimensional discrete dislocation dynamics (DDD) simulations, but these simulations were also performed under unrealistically high bulk hydrogen content ($5 \times 10^4 \sim 10^5$ atm ppm) [54,55]. Excluding the crack tip where high hydrogen accumulation is expected [8,56], we could not find any literatures that directly observed the elastic shielding effect on edge dislocations in BCC steels. The effect of hydrogen on edge dislocation was also studied using first-principles calculations, and both the increased mobility (positive HELP effect) [57] and the decreased mobility (negative HELP effect) [58,59] were reported. Furthermore, the review paper by Feaugas et al. [60] stated the importance of hydrogen effect on the mobility of screw dislocations in BCC metals. Tabata et al. [61] performed in situ TEM observations of pure Fe during tensile straining under a hydrogen gas environment and reported that the velocity of screw dislocations increased with an increase in hydrogen gas pressure. Due to the absence of hydrostatic stress fields, it is considered that screw dislocations do not have any direct elastic interaction with hydrogen atoms. However, Itakura et al. [62], Wen et al. [63] and Kirchheim [64] reported that hydrogen reduced the activation energy for kink-pair nucleation which led to a decrease in the critical shear stress for screw dislocation motion. In the calculation condition performed by Itakura et al., the diffusible hydrogen content was 0.1–10 atm ppm, which covers the experimental condition in the present study (8.9 atm ppm). Yu et al. [65] performed three-dimensional DDD simulations using a realistic bulk hydrogen concentration (0.1 atm ppm). Their results indicated the increased relative velocity of screw dislocation to edge dislocation, resulting in more circular dislocation loops under the presence of hydrogen than the screw-segment-elongated loops without hydrogen. Based on the results, they concluded that hydrogen increased screw dislocation mobility and the contribution of elastic shielding effect on edge dislocations was negligible. Accordingly, a positive HELP effect on screw dislocations could be present (especially at the initial stage of deformation), while a positive HELP effect on edge dislocations would be negligible at least for the experimental condition in the present study. Therefore, we can consider that the tangled dislocation morphology in the hydrogen-charged specimen resulted from the frequent cutting of screw dislocations due to the increase in their velocity.

As shown in Fig. 12, the misorientation of the LEDS boundaries beneath the quasi-cleavage surface was significantly smaller than those 1 mm from the crack tip in the hydrogen-charged specimen. Tabata [56] performed in situ TEM observations on pure Fe under constant tensile stress and reported that the dislocations piled-up on and constituted LEDS boundaries in vacuum condition started to move and overcame the stress field of the boundaries after the hydrogen gas injection (26 kPa). It is assumed that the high hydrogen accumulation around the crack surface significantly reduced the elastic interactions between dislocations (positive HELP), resulting in less misorientation in the LEDS boundaries beneath the quasi-cleavage surface. However, the exact formation mechanism of the LEDS boundaries with a significantly small misorientation remains unclear.

The three characteristics of plastic deformation behavior in the hydrogen-charged specimens: (i) accelerated screw dislocation motion, (ii) tangled dislocation morphology even at the initial stage of deformation (Fig. 8), and (iii) large screw dislocation density at the later stage of deformation (Fig. 3(b)) were explained. These characteristics suggest that jog-dragging by screw dislocations occurred frequently in the hydrogen-charged specimens, leading to the formation of a large number of vacancies on the {011} slip planes. Matsumoto et al. [66] performed first-principles calculations and reported that hydrogen increased the activation energy for vacancy diffusion, resulting in the reduced diffusivity of vacancies. They showed that vacancies nucleated by jog-dragging by screw dislocations remained at a high density in the vicinity of the slip planes. Other literatures also reported that hydrogen stabilized vacancies and vacancy clusters in FCC structures [67–70]. Fig. 13 presents SEM-BSE images of the area around the crack tip in the hydrogen-charged specimen (e = 24%): (a) low magnification and (b) an enlarged view of the rectangular area in (a). The traces of the {011} planes obtained from the EBSD orientation analysis of the corresponding area are indicated by the white dotted lines in Fig. 13(b). Some of the voids coalesced with each other, leading to discontinuous micro-cracks parallel to the {011} plane traces. Lynch et al. [71,72] proposed the void nucleation, growth, and coalescence mechanism in hydrogen-related fracture. In addition, they indicated that, under hydrogen circumstance, void nucleation could be facilitated by vacancy clusters. Doshida et al. [73] used positron probe microanalyzer and reported the higher density of

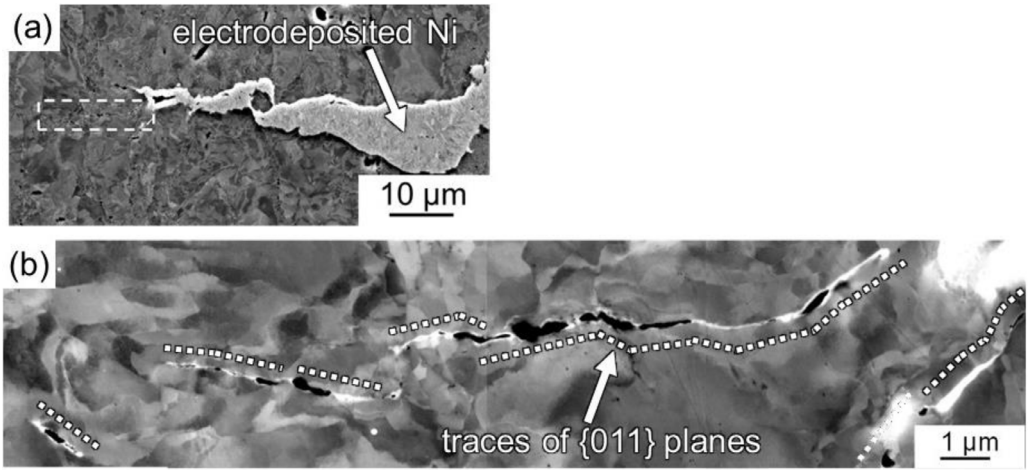

Fig. 13. (a) Low magnification and (b) high magnification BSE images around the crack tip in the hydrogen-charged specimen at a strain amount of 24%. (b) An enlarged view of the rectangular area indicated by the white broken lines in (a). Traces of the {011} planes, white dotted lines in (b), are obtained from EBSD orientation analysis of the corresponding area.

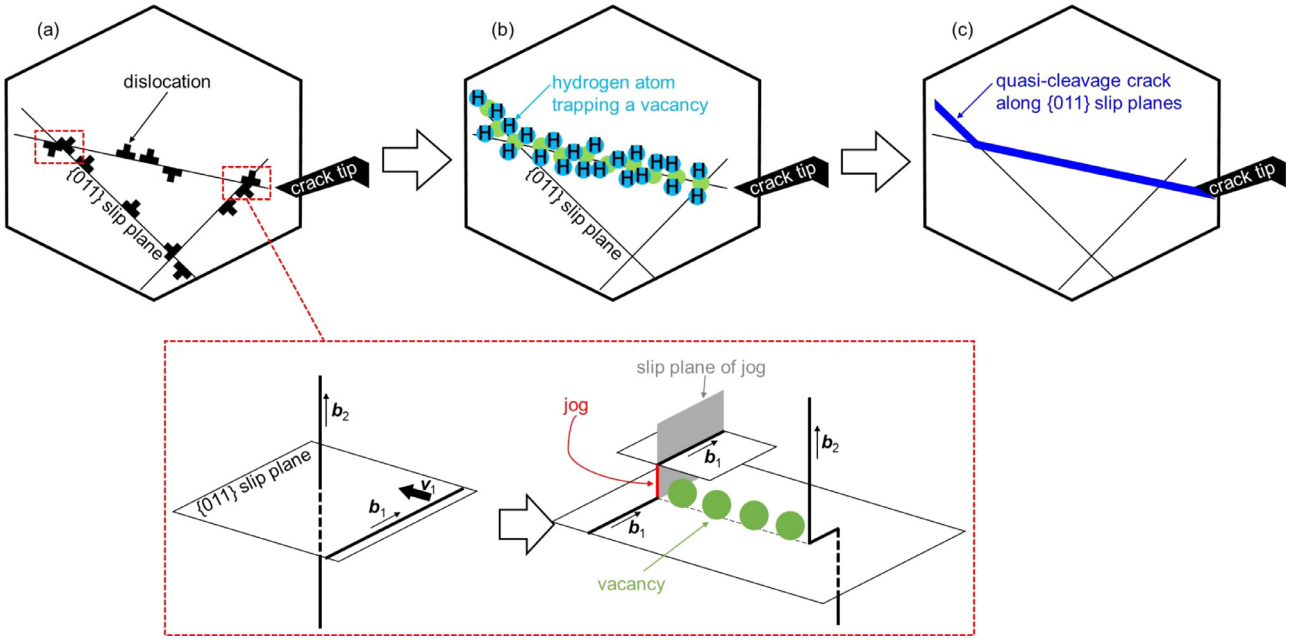

Fig. 14. Schematic illustrations showing the proposed mechanism explaining the hydrogen-related quasi-cleavage fracture along the {011} slip planes in the ferritic steel. (a) Vacancies are frequently nucleated by jog-dragging of screw dislocations. (b) Hydrogen hinders the diffusion of vacancies. Vacancies remain at a high density in the vicinity of {011} slip planes. (c) Vacancies or nanovoids coalesced with each other, leading to the hydrogen-related quasi-cleavage fracture macroscopically along {011} slip planes.

vacancies or vacancy clusters in the region near hydrogen-related quasi-cleavage fracture surface than in other regions in a tempered martensitic steel. Neeraj et al. [74] also reported nanoscale dimples on hydrogen-related quasi-cleavage fracture surfaces of the ferritic-pearlitic steel using SEM under surface-sensitive imaging conditions (low operating voltage: 3–7 kV) and atomic force microscopy. According to the previous studies, it can be considered that the hydrogen-related crack propagation by void coarescense was due to the high density of vacancies or vacancy clusters introduced by jog dragging of screw dislocations in the present steel. In addition, double cross slip of screw dislocations and annihilation of edge dislocation dipoles can also be considered as vacancy nucleation processes during plastic deformation. Vacancies are nucleated along the slip planes by these processes, which is the same as jog dragging of screw dislocations.

Based on the above discussion, we proposed a mechanism explaining the hydrogen-related quasi-cleavage fracture along the {011} slip planes using combination of HELP and HESIV models (Fig. 14). In the hydrogen-charged specimen, vacancies are frequently nucleated by jog-dragging of screw dislocations (Fig. 14(a)). Then, hydrogen suppresses the diffusion of vacancies, and the vacancies remain at a high density in the vicinity of the {011} slip planes (Fig. 14(b)). These vacancies or nanovoids coalesce with each other (Fig. 14(c)). It should be noted that quasi-cleavage fracture does not occur on the atomic {011} plane; rather we propose that the coalescence of a large number of vacancies or nanovoids leads to a quasi-cleavage fracture macroscopically along the {011} slip planes.

5. Summary

In this study, the effect of hydrogen on the evolution of the deformation microstructure in a 2Mn-0.1C steel mainly composed of ferrite microstructure was systematically investigated. The major conclusions are as follows:

I. The dislocation densities derived from neutron diffraction analysis were similar in the hydrogen-charged specimen and the uncharged specimen at each strain amount. However, there was a larger amount of dislocation constituting the LEDS boundaries in the hydrogen-charged specimen and a certain amount of those dislocations were excluded in the dislocation densities derived from neutron diffraction analysis. Consequently, the densities of the total dislocations (existing outside the LEDS boundaries and constituting LEDS boundaries) were higher in the hydrogen-charged specimens.

II. In the uncharged specimen, the fraction of screw dislocations was significantly large ($\sim$ 97%) at the initial stage of deformation (e = 3%). This originated from the dislocation loops that evolved into a screw-segment-elongated morphology owing to the relatively larger velocity of the non-screw segment. The fraction of edge dislocations increased with increasing strain.

III. In the hydrogen-charged specimen, the fraction of edge dislocations was much higher than that in the uncharged specimen at the initial stage of the deformation (e = 3%) due to the increased relative velocity of screw dislocations to edge dislocations in the presence of hydrogen. This further led to the frequent cutting of screw dislocations and tangled dislocation morphology. In addition, the screw dislocation density was much higher in the hydrogen-charged specimen at the later stage of deformation (e = 20%).

IV. In the hydrogen-charged specimen, vacancies were frequently nucleated by the jog-dragging of screw dislocations along the {011} slip planes. Hydrogen hindered the diffusion of vacancies leading to a high density of vacancies in the vicinity of the {011} slip planes. These vacancies or nanovoids coalesced with each other, leading to a hydrogen-related quasi-cleavage fracture not on the atomic {011} plane but macroscopically along the {011} slip planes.

Declaration of Competing Interest

The authors declare that they have no known competing financial interests or personal relationships that could have appeared to influence the work reported in this paper.

Acknowledgement

This study was financially supported by JSPS KAKENHI Grant Numbers JP19J21267, JP15H04158, JP19H02459, and JP20K21083, and the Elements Strategy Initiative for Structural Materials (ESISM) through the Ministry of Education, Culture, Sports, Science and Technology (MEXT), Japan. The neutron diffraction experiment at the Materials and Life Science Experimental Facility of the J-PARC was performed under a user program (Proposal No. 2018A0051). We would like to thank Editage (www.editage.com) for English language editing.

References

[1] A.S. Tetelman, W.D. Roberson, Direct observations and analysis of crack propagation in iron-3% silicon single crystal, Acta Metall. 11 (1963) 415–426.
[2] C.A. Zapffe, C.E. Sims, Hydrogen embrittlement, initial stress and defects in steel, Trans. AIME 145 (1941) 225–261.
[3] W.W. Gerberich, Y.Y. Chen, Hydrogen-controlled cracking – an approach to threshold stress intensity, Metall. Trans. A 6 (1975) 271–278.
[4] R.A. Oriani, H. Josephic, Equilibrium aspects of hydrogen induced cracking of steels, Acta Metall. 22 (1974) 1065–1074.
[5] A. Oriani, H. Josephic, Equilibrium and kinetic studies of the hydrogen assisted cracking of steel, Acta Metall. 25 (1977) 979–988.
[6] P. Sofronis, K. Birnbaum, Mechanics of the hydrogen dislocation impurity interactions I. Increasing shear modulus, J Mech. Phys. Solids 43 (1995) 49–90.
[7] H.K. Birnbaum, P. Sofronis, Hydrogen enhanced localized plasticity a mechanism for hydrogen related fracture, Mater. Sci. Eng. A 176 (1994) 191–202.
[8] T. Tabata, H.K. Birnbaum, Direct observations of hydrogen enhanced crack propagation in iron, Scr. Metall. 18 (1984) 231–236.
[9] M. Nagumo, Function of hydrogen in embrittlement of high-strength steels, ISIJ Int. 41 (2001) 590–598.
[10] M. Nagumo, H. Matsuda, Function of hydrogen in intergranular fracture of martensitic steels, Philos. Mag. A 82 (2002) 3415–3425.
[11] A. Kimura, H. Kimura, Hydrogen embrittlement in high purity iron single crystals, Mater. Sci. Eng. 77 (1986) 75–83.
[12] S.P. Trasatti, E. Sivieri, F. Mazza, Susceptibility of a X80 steel to hydrogen embrittlement, Mater. Corros. 56 (2005) 111–117.
[13] A.W. Thompson, Fractography and its role in fracture interpretation, Fatigue Fract. Eng. Mater. Struct. 19 (1996) 1307–1316.
[14] S.P. Lynch, A fractographic study of gaseous hydrogen embrittlement and liquid-metal embrittlement in a tempered-martensitic steel, Acta Metall. 32 (1984) 79–90.
[15] M.L. Martin, J.A. Fenske, G.S. Liu, P. Sofronis, I.M. Robertson, On the formation and nature of quasi-cleavage fracture surfaces in hydrogen embrittled steels, Acta Mater. 59 (2011) 1601–1606.
[16] Y.H. Kim, J.W. Morris Jr., The nature of quasi-cleavage fracture in tempered 5.5 Ni steel after hydrogen charging, Mater. Trans. A 14 (1983) 1883–1888.
[17] Y.H. Kim, H.J. Kim, J.W. Morris Jr., The influence of precipitated austenite on hydrogen embrittlement in 5.5Ni steel, Metall. Mater. Trans. A 17 (1986) 1157–1164.
[18] A. Nagao, C.D. Smith, M. Dadfarnia, P. Sofronis, I.M. Robertson, The role of hydrogen in hydrogen embrittlement fracture of lath martensitic steel, Acta Mater. 60 (2012) 5182–5189.
[19] A. Shibata, H. Takahashi, N. Tsuji, Microstructural and crystallographic features of hydrogen-related crack propagation in low carbon martensitic steel, Int. ISIJ 52 (2012) 208–212.
[20] A. Shibata, T. Murata, H. Takahashi, T. Matsuoka, N. Tsuji, Characterization of hydrogen-related fracture behavior in as-quenched low-carbon martensitic steel and tempered medium-carbon martensitic steel, Metall. Mater. Trans. A 46 (2015) 5685–5696.
[21] A. Shibata, Y. Momotani, T. Murata, T. Matsuoka, M. Tsuboi, N. Tsuji, Microstructural and crystallographic features of hydrogen-related fracture in lath martensitic steels, Mater. Sci. Technol. 33 (2017) 1524–1532.
[22] K. Okada, A. Shibata, Y. Takeda, N. Tsuji, Crystallographic feature of hydrogen-related fracture in 2Mn-0.1C ferritic steel, Int. J. Hydrogen Energy 43 (2018) 11298–11306.
[23] K. Takai, H. Shoda, H. Suzuki, M. Nagumo, Lattice defects dominating hydrogen-related failure of metals, Acta Mater. 56 (2008) 5158–5167.
[24] T. Ungar, I. Dragomir, A. Revesz, A. Borbely, The contrast factors of dislocations in cubic crystals: the dislocation model of strain anisotropy in practice, J Appl. Cryst. 32 (1999) 992–1002.
[25] G. Ribarik, T. Ungar, Characterization of the microstructure in random and textured polycrystals and single crystals by diffraction line profile analysis, Mater. Sci. Eng. A 528 (2010) 112–121.
[26] G. Ribarik, J. Gubicza, T. Ungar, Correlation between strength and microstructure of ball-milled Al–Mg alloys determined by X-ray diffraction, Mater. Sci. Eng. A 387-389 (2004) 343–347.
[27] K. Murasawa, M. Takamura, M. Kumagai, Y. Ikeda, H. Suzuki, Y. Otake, T. Hama, S. Suzuki, Determination approach of dislocation density and crystallite size using a convolutional multiple whole profile software, Mater. Trans. 59 (2018) 1135–1141.
[28] S.M. Al-Jubouri, B.I. Waisi, S.M. Holmes, Rietveld texture refinement analysis of linde type a zeolite from X-ray diffraction data, J. Eng. Sci. Technol. 13 (2018) 4066–4077.
[29] T. Ungar, H. Mughrabi, D. Ronnpagel, M. Wilkens, X-ray line-broadening study of the dislocation cell structure in deformed [011]-oriented copper single crystals, Acta Metall. 32 (1984) 333–342.
[30] S. Harjo, T. Kawasaki, Y. Tomota, W. Gong, K. Aizawa, G. Tichy, Z. Shi, T. Ungar, Work hardening, dislocation structure, and load partitioning in lath martensite determined by in situ neutron diffraction line profile analysis, Metall. Mater. Trans. A 48 (2017) 4080–4092.
[31] B.L. Adams, J. Kacher, EBSD-based microscopy: resolution of dislocation density, CMC 14 (2009) 185–196.
[32] S. Wang, N. Hashimoto, Y. Wang, S. Ohnuki, Activation volume and density of mobile dislocations in hydrogen-charged iron, Acta Mater. 61 (2013) 4734–4742.
[33] X. Huang, G. Winther, Dislocation structures. Part I. Grain orientation dependence, Philos. Mag. 87 (2007) 5189–5214.
[34] Q. Liu, D. Juul Jensen, N. Hansen, Effect of grain orientation on deformation structure in cold-rolled polycrystalline aluminium, Acta Mater. 46 (1998) 5819–5838.
[35] X. Huang, Grain orientation effect on microstructure in tensile strained copper, Scr. Mater. 38 (1998) 1697–1703.
[36] A. Haldar, X. Huang, T. Leffers, N. Hansen, R.K. Ray, Grain orientation dependence of microstructures in a warm rolled IF steel, Acta Mater. 52 (2004) 5405–5418.
[37] S. Wang, A. Nagao, P. Sofronis, I.M. Robertson, Hydrogen-modified dislocation structures in a cyclically deformed ferritic-pearlitic low carbon steel, Acta Mater. 144 (2018) 164–176.
[38] E.I. Galindo-Nava, P.E.J. Rivera-Diaz-del-Castillo, Modelling plastic deformation in BCC metals: dynamic recovery and cell formation effects, Mater. Sci. Eng. A 558 (2012) 641–648.
[39] R.E. Smallman, R.J. Bishop, Modern Physical Metallurgy and Materials Engineering, Butterworth-Heinemann, 1999 (book).
[40] E.I. Galindo-Nava, P.E.J. Rivera-Diaz-del-Castillo, A thermodynamic theory for dislocation cell formation and misorientation in metals, Acta Mater. 60 (2012) 4370–4378.
[41] M.R. Staker, D.L. Holt, The dislocation cell size and dislocation density in cupper deformed at temperatures between 25 and 700°C, Acta Metall. 20 (1970) 569–579.
[42] G. Girardin, C. Huvier, D. Delafosse, X. Feaugas, Correlation between dislocation organization and slip bands: TEM and AFM investigations in hydrogen-containing nickel and nickel–chromium, Acta Mater. 91 (2015) 141–151.
[43] S. Wang, A. Nagao, K. Edalati, Z. Horita, I.M. Robertson, Influence of hydrogen on dislocation self-organization in Ni, Acta Mater. 135 (2017) 96–102.
[44] Z.D. Harris, S.K. Lawrence, D.L. Medlin, G. Guetard, J.T. Burns, B.P. Somerday, Elucidating the contribution of mobile hydrogen-deformation interactions to hydrogen-induced intergranular cracking in polycrystalline nickel, Acta Mater. 158 (2018) 180–190.
[45] A. Oudriss, X. Feaugas, Length scales and scaling laws for dislocation cells developed during monotonic deformation of (001) nickel single crystal, Int. J Plast. 78 (2016) 187–202.
[46] I.M.A. Ghermaoui, A. Oudriss, A. Metsue, R. Milet, K. Madani, X. Feaugas, Multiscale analysis of hydrogen-induced softening in f.c.c. nickel single crystals oriented for multiple-slips: elastic screening effect, Sci. Rep. 9 (13042) (2019) 13042.
[47] B. Sestak, N. Zarubova, V. Sladek, Slip planes in Fe –3% Si single crystals deformed at 77K, Can. J. Phys. 45 (1967) 1031–1040.
[48] T. Taoka, S. Takeuchi, E. Furubayashi, Slip systems and their critical shear stress in 3% silicon iron, J Phys. Soc. Jpn. 19 (1964) 701–711.
[49] E. Furubayashi, Behavior of dislocations in Fe-3% Si under stress, J Phys. Soc. Jpn. 27 (1969) 130–146.
[50] L.P. Kubin, F. Louchet, Analysis of softening in the Fe-C system from in situ and conventional experiments – I. In situ experiments, Acta Metall. 27 (1979) 337–342.
[51] J.W. Christian, Some surprising features of the plastic deformation of body–centered cubic metals and alloys, Metall. Trans. A 14 (1983) 1237–1256.
[52] L.P. Kubin, The low-temperature mechanical properties of BCC metals and their alloys – II, Rev. Deform. Behav. Mater. 1 (1976) 244–288.
[53] D. Caillard, Kinetics of dislocations in pure Fe. Part I. In situ straining experiments at room temperature, Acta Mater. 58 (2010) 3493–3503.
[54] W. Cai, V.V. Bulatov, Mobility laws in dislocation dynamics simulations, Mater. Sci. Eng. A 387-389 (2014) 277–281.
[55] Y. Gu, J.A. El-Awady, Quantifying the effect of hydrogen on dislocation dynamics: a three-dimensional discrete dislocation dynamics framework, J. Mech. Phys. Solids 112 (2018) 491–507.
[56] T. Tabata, Direct observation of the effect of hydrogen on the mechanical properties of iron, Bull. Jpn. Inst. Metals 24 (1985) 485–493.
[57] S. Wang, N. Hashimoto, S. Ohnuki, Hydrogen-induced change in core structures of {110}[111]edge and {110}[111]screw dislocations in iron, Sci. Rep. 3 (2760) (2013) 2760.
[58] S. Taketomi, R. Matsumoto, N. Miyazaki, Atomistic study of the competitive relationship between edge dislocation motion and hydrogen diffusion in alpha iron, J. Mater. Res. 26 (2011) 1269–1278.
[59] M.F. Kapci, J.C. Schon, B. Bal, The role of hydrogen in the edge dislocation mobility and grain boundary-dislocation interaction in α-Fe, Int. J. Hydrogen Energy 46 (2021) 32695–32709, doi:10.1016/j.ijhydene.2021.07.061.

[60] X. Feaugas, D. Delafosse; 9 - Hydrogen and crystal defects interactions: effects on plasticity and fracture, mechanics - microstructure - corrosion coupling, (2019), pp. 199–222.
[61] T. Tabata, H.K. Birnbaum, Direct observations of the effect of hydrogen on the behavior of dislocations in iron, Scr. Metall. 17 (1983) 947–950.
[62] M. Itakura, H. Kaburaki, M. Yamaguchi, T. Okita, The effect of hydrogen atoms on the screw dislocation mobility in bcc iron: a first-principles study, Acta Mater. 61 (2013) 6857–6867.
[63] M. Wen, S. Fukuyama, K. Yokogawa, Atomistic simulations of effect of hydrogen on kink-pair energetics of screw dislocations in bcc iron, Acta Mater. 51 (2003) 1767–1773.
[64] R. Kirchheim, Solid solution softening and hardening by mobile solute atoms with special focus on hydrogen, Scr. Mater. 67 (2012) 767–770.
[65] H. Yu, A. Cocks, E. Tarleton, Discrete dislocation plasticity HELPs understand hydrogen effects in bcc materials, J. Mech. Phys. Solids 123 (2019) 41–60.
[66] R. Matsumoto, N. Nishiguchi, S. Taketomi, N. Miyazaki, First-principles calculations of hydrogen effects on the formation and diffusion of vacancies in alpha iron: discussion of the hydrogen-enhanced strain-induced vacancy mechanism, Zairyo 63 (2014) 182–187.
[67] Y. Fukai, Superabundant vacancies formed in metal–hydrogen alloys, Phys. Scr. T103 (2003) 11–14.
[68] S. Miraglia, D. Fruchart, E.K. Hlil, S.S.M. Tavares, D. Dos Santos, Investigation of the vacancy-ordered phases in the Pd–H system, J. Alloys Compd. 317-318 (2001) 77–82.
[69] A. Metsue, A. Oudriss, X. Feaugas, Hydrogen solubility and vacancy concentration in nickel single crystals at thermal equilibrium: new insights from statistical mechanics and ab initio calculations, J. Alloys Compd. 656 (2016) 555–567.
[70] M.G. Ganchenkova, Y.N. Yagodzinskyy, V.A. Borodin, H. Hänninen, Effects of hydrogen and impurities on void nucleation in copper: simulation point of view, Philos. Mag. 94 (2014) 3522–3548.
[71] S.P. Lynch, Discussion of some recent literature on hydrogen-embrittlement mechanisms: addressing common misunderstandings, Corros. Rev. 37 (2019) 377–395.
[72] S.P. Lynch, Hydrogen embrittlement phenomena and mechanisms, Corros. Rev. 30 (2012) 105–123.
[73] T. Doshida, H. Suzuki, K. Takai, N. Oshima, T. Hirade, Enhanced lattice defect formation associated with hydrogen and hydrogen embrittlement under elastic stress of a tempered martensitic steel, ISIJ Int. 52 (2012) 198–207.
[74] T. Neeraj, R. Srinivasan, J. Li, Hydrogen embrittlement of ferritic steels: observations on deformation microstructure, nanoscale dimples and failure by nanovoiding, Acta Mater. 60 (2012) 5160–5171.